Materials and Design 118 (2017) 304–313

Contents lists available at ScienceDirect

Materials and Design

journal homepage: www.elsevier.com/locate/matdes

Microstructure statistics–property relations of silver particle-based interconnects

A. Gillman[a], M.J.G.H. Roelofs[b], K. Matouš[a], V.G. Kouznetsova[b,*], O. van der Sluis[b,c], M.P.F.H.L. van Maris[b]

[a]Department of Aerospace and Mechanical Engineering, University of Notre Dame, Notre Dame, IN 46556, USA
[b]Department of Mechanical Engineering, Eindhoven University of Technology, PO Box 513, Eindhoven, 5600 MB The Netherlands
[c]Philips Research Laboratories, High Tech Campus 4, 5656 AE Eindhoven, The Netherlands

HIGHLIGHTS

- A novel approach for microstructure statistics-property relations for a silver particle-based thermal interface material
- The methodology combines the higher-order statistical micromechanics and finite element computational homogenization
- 3D microstructure is revealed by Focused Ion Beam – Scanning Electron Microscopy (FIB-SEM) technique
- The relation between the processing conditions, statistical microstructural features and effective materials properties
- The methodology will lead to the increased efficiency of material development

GRAPHICAL ABSTRACT

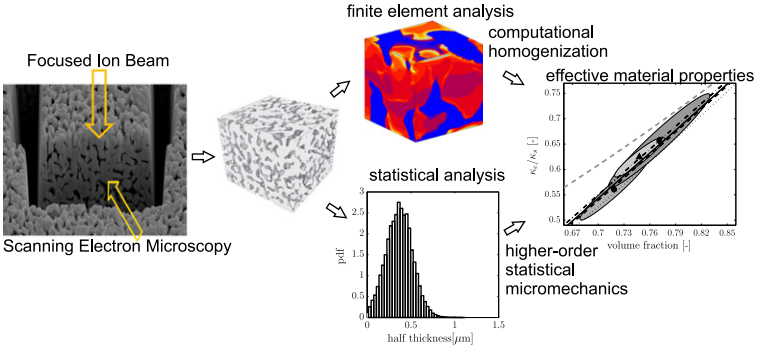

ARTICLE INFO

Article history:
Received 5 October 2016
Received in revised form 23 December 2016
Accepted 3 January 2017
Available online 11 January 2017

Keywords:
Structure-property relations
Statistical micromechanics
Computational homogenization
Sintered silver
Thermal interface material
SEM-FIB

ABSTRACT

This paper presents a novel approach for establishing microstructure statistics-property relations for a silver particle-based thermal interface material (TIM). Several sintered silver TIMs have been prepared under different processing conditions, generating samples with distinct microstructures. The 3D microstructure is revealed and visualized using the combination of Focussed Ion Beam (FIB) milling and Scanning Electron Microscopy (SEM) imaging. Representative synthetic model microstructures have been generated based on Gaussian random field models, having well defined analytical descriptions. The statistical characteristics of the samples and the synthetic models are shown to have a good correspondence, indicating that the linear effective properties of these complex materials can be predicted based on analytical estimates available for the synthetic models. This is verified by computing the effective elastic and thermal material properties using the computational homogenization approach based on the finite element models of the real samples. The computational homogenization, providing the reference solution, and the higher-order statistical estimates for the synthetic models are in very good agreement. These results can be used in the development of new silver particle-based materials, whereby the expensive and time consuming effective material property characterization can be replaced by efficient estimation based on the synthetic random field models.

* Corresponding author.
E-mail address: v.g.kouznetsova@tue.nl (V. Kouznetsova).

http://dx.doi.org/10.1016/j.matdes.2017.01.005
0264-1275/

1. Introduction

The next generation of high power electronic devices, such as high power LEDs, requires thermal interface materials (TIM) that exhibit excellent heat dissipation properties through high thermal conductivity in order to control operating temperatures of the electronic devices [1]. In addition, these materials should have appropriate mechanical properties to prevent reliability issues during the lifetime cycle. Due to their relatively high thermal conductivity, and low temperature processing, sintered silver pastes are of particular interest. During sintering, a porous connected silver structure is generated. Evidently, the processing conditions (e.g., sintering temperature, heating rate, holding time) affect the microstructure of the material and, consequently, the resulting thermal and mechanical properties [2–4]. A common material development practice typically involves multiple trial-and-error cycles: application of expert knowledge-based variations on chemical composition and processing conditions, followed by material inspection by cross-sectioning and time consuming and expensive experimental testing at the material, subsystem and component level. This material development cycle can be significantly shortened by establishing a fundamental understanding of the microstructure statistics-property relations [5].

Several analytical models have been proposed in the literature to predict the thermal and mechanical properties of TIMs. The simplest estimate is given by the rule of mixtures, which is a zeroth-order approximation and includes the volume fraction as the single parameter [1]. This simple approximation can be improved by adding certain idealized assumptions on the microstructure of the material, e.g. particle or pore shape (usually spherical or ellipsoidal), distribution, orientation, packing, etc. [6–9]. Although these models can match the experimental values, they usually require some fitting and thus do not establish a direct relation between microstructural variations and the effective properties. Another approach that leads to very good prediction of the effective properties is based on direct numerical (often finite element) simulations of either idealized [10], or actual microstructures obtained from micrographs (2D) [11–13], or computer tomography (3D) [14]. This is a very powerful and rather accurate technique, however, demanding from the viewpoint of time and computer resources. Although leading to property predictions, it does not always provide insight into the relative contribution of the different microstructural features. Effective material properties can also be obtained using statistical micromechanics theories [15,16]. If a good statistical description of the microstructure is known, e.g. size distribution and configuration of particles, higher-order statistical models can very efficiently and accurately predict the effective material properties [17–19]. For complex, interconnected microstructures with non-trivial 3D geometrical features, the choice of an appropriate statistical model is less straightforward.

In this paper, the microstructure statistics-property relations of silver TIM are established by the novel link between synthetic microstructures (i.e. Gaussian random field and symmetric-cell models) with statistical morphological measures and the higher-order statistical micromechanics. The verification of the thermo-mechanical properties is provided by the computational homogenization of the actual microstructure. This approach opens new pathways for practical material development, where the expensive experimental testing, microscopic material characterization and numerical simulation cycles can be replaced by less expensive and efficient predictions based on the higher-order statistical estimates. This requires identification of a synthetic microstructural model that is statistically representative of the TIM morphology, which in this work has been generated based on Gaussian random field models. We note that the proposed microstructure statistics-property methodology can be applied to other porous/heterogeneous thermal interface materials (e.g., transient liquid phase conductive adhesives) with bicontinuous structures.

The paper is organized as follows. Section 2 summarizes the material processing and 3D microstructure visualization procedure, as well as the generation of the synthetic microstructures. The statistical characterization of the real and synthetic microstructures is performed in Section 3. After a brief summary of the computational homogenization and statistical micromechanics approaches for the effective property estimation in Section 4, the results are presented in Section 5. The paper ends with concluding remarks in Section 6.

2. Material processing and 3D microstructure visualization

The silver-particle based thermal interface material has been provided by Heraeus company [20] in the form of silver particles/flakes in a polymer solvent. Droplets of the material were placed on a glass plate and processed in a Carbolite CSF1200 oven. The processing temperature profile is shown in Fig. 1. The oven was first pre-heated for 1 h to 160 °C to achieve a homogeneous temperature before placing the samples. The first step in the processing is known as “drying”, during which the solvent evaporates and only silver particles remain. Drying was done for 50 min at 160 °C for all samples. The second step is the actual sintering of the silver particles, during which silver particles agglomerate and form a connected structure. To obtain a distinct variation in the microstructure, three different sintering temperatures were used, i.e. 230 °C, 280 °C, 330 °C, resulting in three samples, hereafter labeled S1, S2 and S3, respectively. The sintering time was the same for all the three samples, equal to 60 min. The cool down step was performed inside the oven at a measured rate of 12.5 °C/min.

For the visualization and subsequent characterization of 3D material structure, the SEM-FIB technique [21,22] is applied using the FEI DualBeam system. This imaging technique combines alternating milling of thin slices (in this work 30 nm) of the material using Focused Ion Beam (FIB) and Scanning Electron Microscopy (SEM) imaging. These consecutive SEM images can next be reconstructed to a 3D volume. The SEM-FIB process is illustrated in Fig. 2.

The scanned reconstructed cross-sectional images are segmented to distinguish between pixels representing silver and air. By assigning a thickness to each pixel in the images (corresponding to the thickness of the FIB removed layer), a 3D voxel data set is generated. Fig. 3 shows the segmented 3D visualizations of all three samples; the corresponding voxel data can be found in Table 1. These three 3D visualizations were used for the statistical characterization and effective property estimation as will be discussed in the subsequent sections. Table 1 shows that the volume fraction of the solid phase increases with increasing processing temperature, i.e. porosity decreases.

In addition to these real microstructures, synthetic microstructures having a well defined analytical description are considered

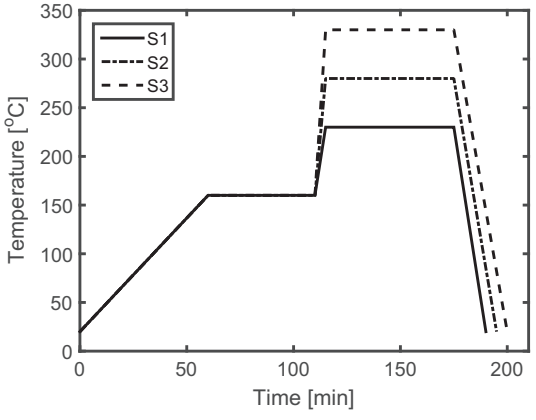

Fig. 1. Processing temperature profile of the three samples.

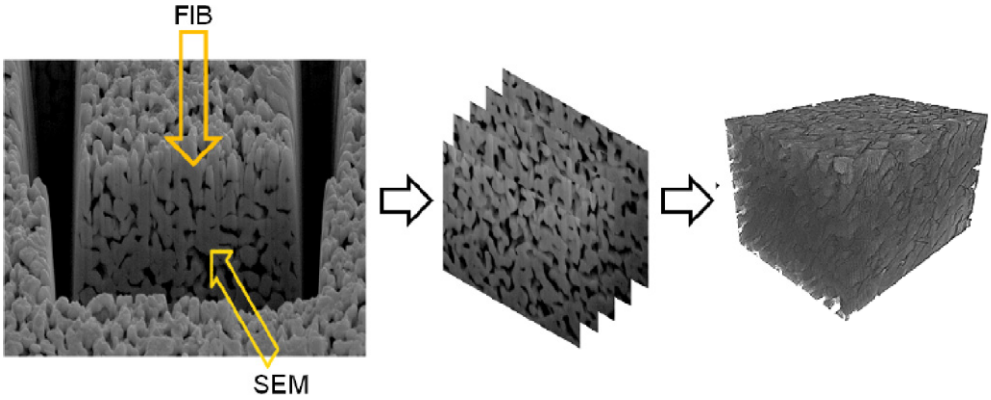

Fig. 2. Illustration of the SEM-FIB procedure leading to 3D visualization of the microstructure of the material.

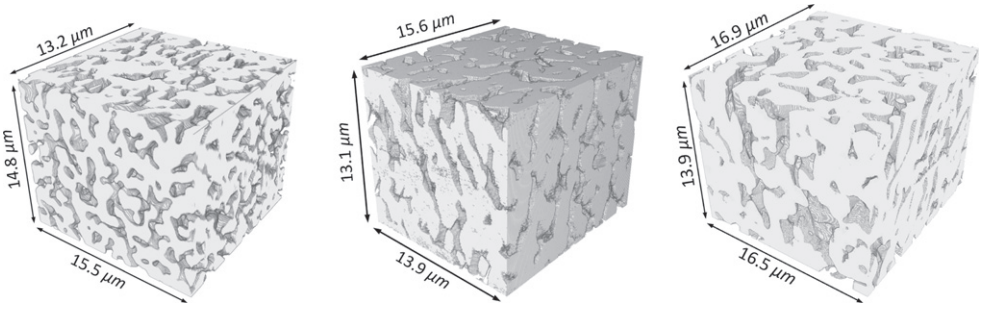

(a) Sample S1 (b) Sample S2 (c) Sample S3

Fig. 3. Segmented 3D visualizations of the three samples obtained by SEM-FIB.

in order to better understand the microstructure statistics-property relations for these silver interconnects. For this purpose, we consider Gaussian random field (GRF) models as introduced by other researchers studying porous materials and microemulsions [23–26]. In this study, we found that a one-cut GRF model proposed by Roberts and Teubner [23] has similar structural characteristics to the porous silver microstructures. In particular, the field-field correlation function, $g(r)$, denoted as Model III in [23] is considered, where

$$g(r) = \frac{3\left(\sin(\mu r) - \mu r\cos(\mu r) - \sin(r) - r\cos(r)\right)}{r^3(\mu^3 - 1)}, \tag{1}$$

and the corresponding spectral density is given as

$$\rho(k) = \frac{3}{4\pi(\mu^3 - 1)}\left(H(k-\mu) - H(k-1)\right). \tag{2}$$

Here, H is the Heaviside function, μ is a free parameter, and r and k are the real spatial and transform variables, respectively. Using the definition of the field-field correlation function, T-periodic Gaussian random fields with a maximum wave number of $K = 2\pi N/T$ can be formulated as

$$y(\boldsymbol{x}) = \sum_{l=-N}^{N}\sum_{m=-N}^{N}\sum_{n=-N}^{N} c_{lmn}\exp(i\boldsymbol{k}_{lmn}\cdot\boldsymbol{x}), \tag{3}$$

Table 1
Voxel data of the visualizations of the three samples.

Sample	Volume [μm³]	Volume fraction of silver [%]	Pixel size [nm]
S1	13.2 × 15.5 × 14.8	71.4	30
S2	13.9 × 15.6 × 13.1	73.9	30
S3	16.9 × 16.5 × 13.9	76.7	30

where i is the imaginary number, and $\boldsymbol{k}_{lmn} = \frac{2\pi}{T}(l\boldsymbol{i} + m\boldsymbol{j} + n\boldsymbol{k})$ with $k = ||\boldsymbol{k}||$. The coefficients c_{lmn} are defined as $c_{lmn} = a_{lmn} + ib_{lmn}$, and a_{lmn} and b_{lmn} are random independent variables from Gaussian distributions, where $\langle a\rangle = \langle b\rangle = 0$ and $\langle a\rangle^2 = \langle b\rangle^2 = \frac{1}{2}\rho(k_{lmn})(2\pi/T)^3$. See [23] for more details. Here, microstructures with 512^3 voxels are generated with a MATLAB script while utilizing MATLAB's fast Fourier transform (FFT) algorithms with $\mu = 1.5$ and $T = 8\pi$. The volume fractions were matched to samples S1–S3 by iteratively selecting the threshold β such that all voxels with function values of $-\infty \le y(\boldsymbol{x}) \le \beta$ are set to 1 (solid material phase), and all other voxels equal 0 (void phase). A qualitative comparison is made in Fig. 4 for sample S3. For the remainder of the paper, S#-FIB and S#-GRF will be used to differentiate between the real and synthetic microstructures, respectively. The pixel size was determined by minimizing the difference in the two-point probability function, $S_{qs}(r = |\boldsymbol{Y} - \boldsymbol{Y}'|)$, of the real and synthetic microstructures [27]

$$\Pi(\alpha) = ||S_{ss,\text{real}}(r) - S_{ss,\text{synthetic}}(\alpha\, r)||. \tag{4}$$

Here $S_{ss,\text{real}}(r)$ is the two-point probability function of the real microstructure (FIB) where the subscript s represents the solid phase, $S_{ss,\text{synthetic}}(\alpha\, r)$ is the function for the synthetic GRF microstructure, and α is the pixel size of the synthetic GRF model and the variable being optimized. This optimization variable results in a horizontal scaling or stretching of the two-point probability function. Results of the two-point point probability functions are discussed in further detail in the following section. Note that the pixel size or scale of the synthetic microstructures is considered here to simply scale the numerically generated structures for consistent comparison of various statistical morphological measures. It should be noted that the scaling has no impact on the effective property predictions of materials with linear constitutive relations. The resulting domain sizes

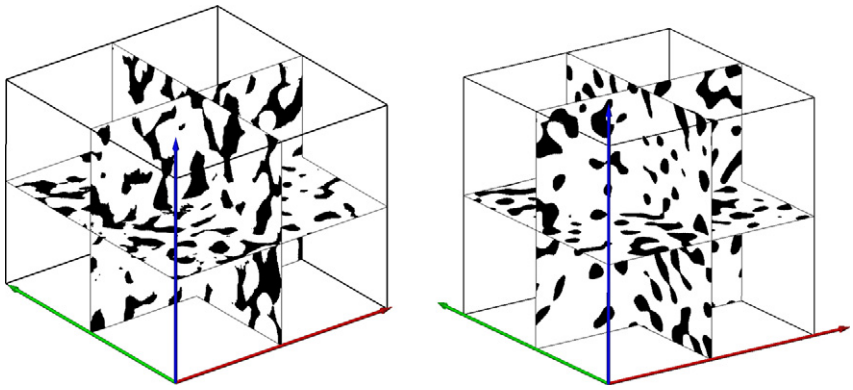

(a) S3-FIB (real) (b) S3-GRF (synthetic)

Fig. 4. Comparison of orthoslices for (a) real silver microstructure and (b) synthetic Gaussian random field (GRF).

and pixel sizes for the generated synthetic microstructures are summarized in Table 2. Finally we note, that developing and tuning a field-field function to match multiple structural characteristics (e.g., second-point correlations, filament thickness distribution, minimum distance field, etc.) is an active area of research. Thus microstructure statistics-property relations play an important role for future development of new field-field functions designed specifically for these materials.

3. Statistical characterization

Probability functions (n-point), $S_{qs\cdots t}(\boldsymbol{x}_1, \boldsymbol{x}_2, \cdots, \boldsymbol{x}_n)$, are commonly used statistical descriptors that quantify complex microstructures [16,17,27]. These functions represent the probability of phases $q, s, \cdots, t$ existing at points $\boldsymbol{x}_1, \boldsymbol{x}_2, \cdots, \boldsymbol{x}_n$ and are defined as

$$S_{qs\cdots t}(\boldsymbol{x}_1, \boldsymbol{x}_2, \cdots, \boldsymbol{x}_n) = \chi_q(\boldsymbol{x}_1)\chi_s(\boldsymbol{x}_2)\cdots\chi_t(\boldsymbol{x}_n). \quad (5)$$

Here, $\chi_q(\boldsymbol{x})$ is the indicator function, and the overbar signifies an ensemble average (equivalent to volume averaging when assuming ergodicity). In this work, the two-point probability function quantifies the short- and long-range character of these complex porous microstructures and are computed using our in-house parallel statistical sampling code, *Stat3D* [17-19,27]. The two-point probability functions, S_{ss}, for the real and synthetic microstructures are shown in Fig. 5. It can be observed that the shape of these functions is similar for both the real and synthetic microstructures. The similarities suggest that GRF models are suitable for representing the porous silver interconnect materials. In addition, the functions saturate at $r_{sat} = 5\mu$m, which suggests a representative cell size $2 \times r_{sat}$. Note that all synthetic and real microstructures have domain lengths larger than this characteristic size (see Tables 1 and 2).

In order to further quantify the local structures, image processing and analysis have been performed. In Fig. 3, interconnected bicontinuous structures are observed. Therefore, an image processing pipeline similar to the one described in Shuck et al. [22] is utilized to quantify the thicknesses of the ligament structures throughout the voxel data set. The software package *AvizoFire* (FEI) is employed for image processing. The image processing pipeline is illustrated for sample S1-FIB in Fig. 6. The processing pipeline begins with the thresholded binary data set (A in Fig. 6). A skeletonization algorithm [28] is performed in two steps. First, a thinning algorithm peels back the surface of the binary data set until a structure with one voxel thickness remains. Note that the thinning algorithm results in a line of voxels for filament structures, and a shell remains around fully enclosed holes (see B in Fig. 6). Second, the thinned structure is smoothed until only ligaments of voxels remain (see C in Fig. 6). A chamfer minimum distance map is also computed from the input binary image data (see D in Fig. 6). The chamfer distance field represents the minimum Euclidean distance from a point within the material to the material/void interface. The resulting distance field is then multiplied by the binary image of the thinned structure (B × D results in E in Fig. 6), and the resulting dataset represents the half thickness of each point in the skeleton. The image processing pipeline is performed for all real and synthetic microstructures.

Following the image-processing pipeline described above, the distribution of the average thickness (two times the half thickness distribution) is determined for the real and synthetic microstructures. The resulting probability density function (pdf) distributions are shown in Fig. 7. The minimum, mean, and maximum thickness are also indicated in these figures. Comparing the thickness distributions between the three real samples, Fig. 7 (a, b), it can be observed that the mean ligament thickness and the width of the ligament

Table 2
Domain descriptions for GRF samples with pixel sizes obtained from minimization problem defined in Eq. (4).

Sample	Volume [μm³]	Volume fraction of silver [%]	Pixel size [nm]
S1-GRF	10.7 × 10.7 × 10.7	71.4	20.9
S2-GRF	12.5 × 12.5 × 12.5	73.9	24.5
S3-GRF	12.6 × 12.6 × 12.6	76.7	24.7

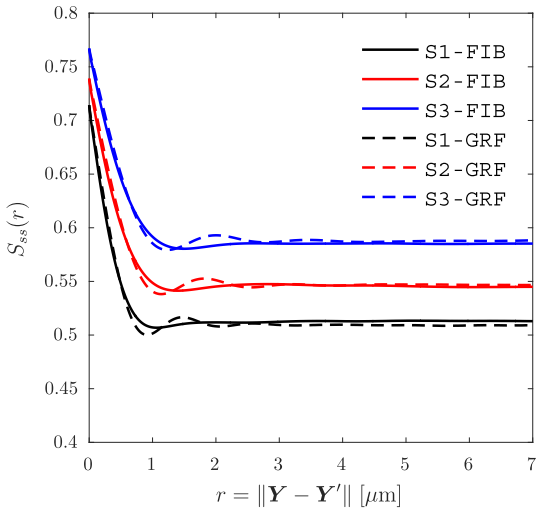

Fig. 5. Isotropic two-point probability function for the solid phase, S_{ss}.

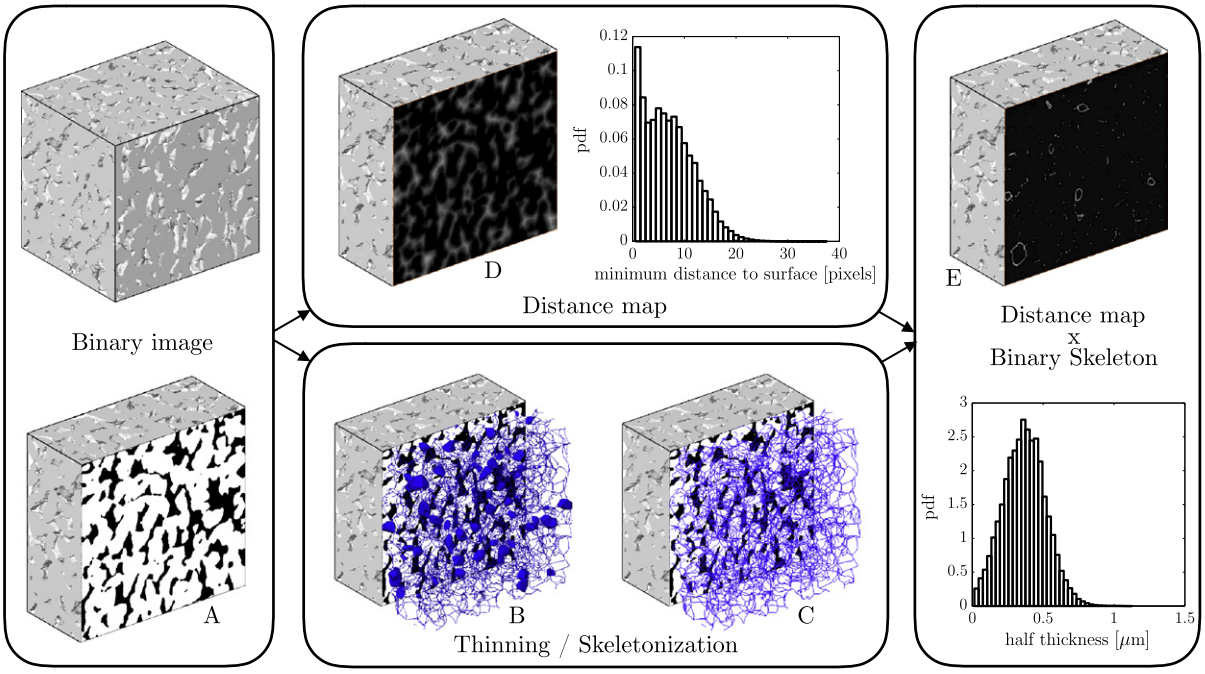

Fig. 6. Overview of the image processing pipeline: Voxel datasets are processed using FEI's AvizoFire in order to quantify the structure of the morphology.

thickness distribution increase between the samples S1 and S2, while the difference between the samples S2 and S3 is very small. The thickness distributions of the real (Fig. 7 (a, b)) and GRF (Fig. 7 (c, d)) microstructures are very similar. The synthetic GRF distributions preserve the trend in the mean, with the mean thickness increasing for microstructures having larger volume fractions (S1 has lowest volume fraction, and S3 has largest volume fraction), although the difference between the synthetic S2-GRF and S3-GRF is slightly larger than for the real structures S2-FIB and S3-FIB.

The structure of the resulting skeletons (see image data C in Fig. 6, for example) are analysed. The number of nodes (cross-point vertices) and edges (ligaments) in the skeletons is reported in Fig. 8, where the quantities are normalized by the volume V of the data set. Note that the monotonic decrease of the no. of edges/vertices in samples S1–S3 (increasing volume fraction) is captured for both the real and synthetic microstructures. However, the density of the edges/vertices is higher for the GRF samples. This is likely due to the increasing number of average sized ligaments in the synthetic microstructures, i.e. the probability of the mean thickness is higher for the synthetic (GRF) microstructures (higher pdf values in Fig. 7 (d) compared to pdf values in Fig. 7 (b)).

Based on the statistical analysis presented in this section, it can be concluded that the generated Gaussian random field synthetic microstructures can be considered statistically representative for the sintered silver material. Consequently, the synthetic models can be used for the prediction of the linear effective material properties of sintered silver interconnect materials, thus avoiding (or minimizing) the expensive material characterization. This hypothesis will be verified in the following.

4. Thermo-mechanical property estimates

The thermo-mechanical properties of the silver paste interconnect materials have been computed numerically, based on the computational homogenization approach, providing the reference solution, and by statistical micromechanics theories.

4.1. Computational homogenization for effective material properties

Computational homogenization is by now a well established technique for computing the macroscopic (effective) properties of heterogeneous materials, including non-linear behavior and evolving microstructures. A general review on the computational homogenization technique and the implementation details can be found in references [29,30], among others.

The computational homogenization technique is based on the construction and solution of a detailed microstructural model. In this work, microstructural models were obtained by cutting out windows of various sizes from the 3D reconstructed and segmented microstructures, see Fig. 9. These models will be here referred to as Microstructural Volume Elements (MVE). To create finite element models of these MVEs, each voxel within an MVE has been transformed to a (hexahedron) finite element. Based on the segmentation, the finite element was assigned material properties of either silver or "air", given in Table 3. Note, that for the silver phase, material properties of bulk silver have been taken, due to the lack of material data for nano-particle silver. The material properties of "air" have been selected to represent a phase with thermal conductivity and stiffness properties negligibly low compared to the metal phase. The material properties have been assumed temperature independent in the temperature range relevant for the application of the interconnect materials (approx. −40 °C to 150 °C).

For the computation of the effective thermal conductivity, MVEs were subjected to an overall macroscopic temperature gradient, in combination with the periodic boundary conditions, see [13,31] for details. Note, that the use of the periodic boundary conditions results in a non-uniform, but periodic, temperature distribution on the cube faces. This provides less thermal constraints and is known to lead to better estimation of the effective thermal conductivity compared to fully prescribing temperature on the whole face (giving overestimation of the effective thermal conductivity) or prescribing the thermal flux (giving underestimation) [32]. In this work, the temperature gradient in the vertical direction of the images was prescribed; it has been verified that prescribing a temperature gradient in the other

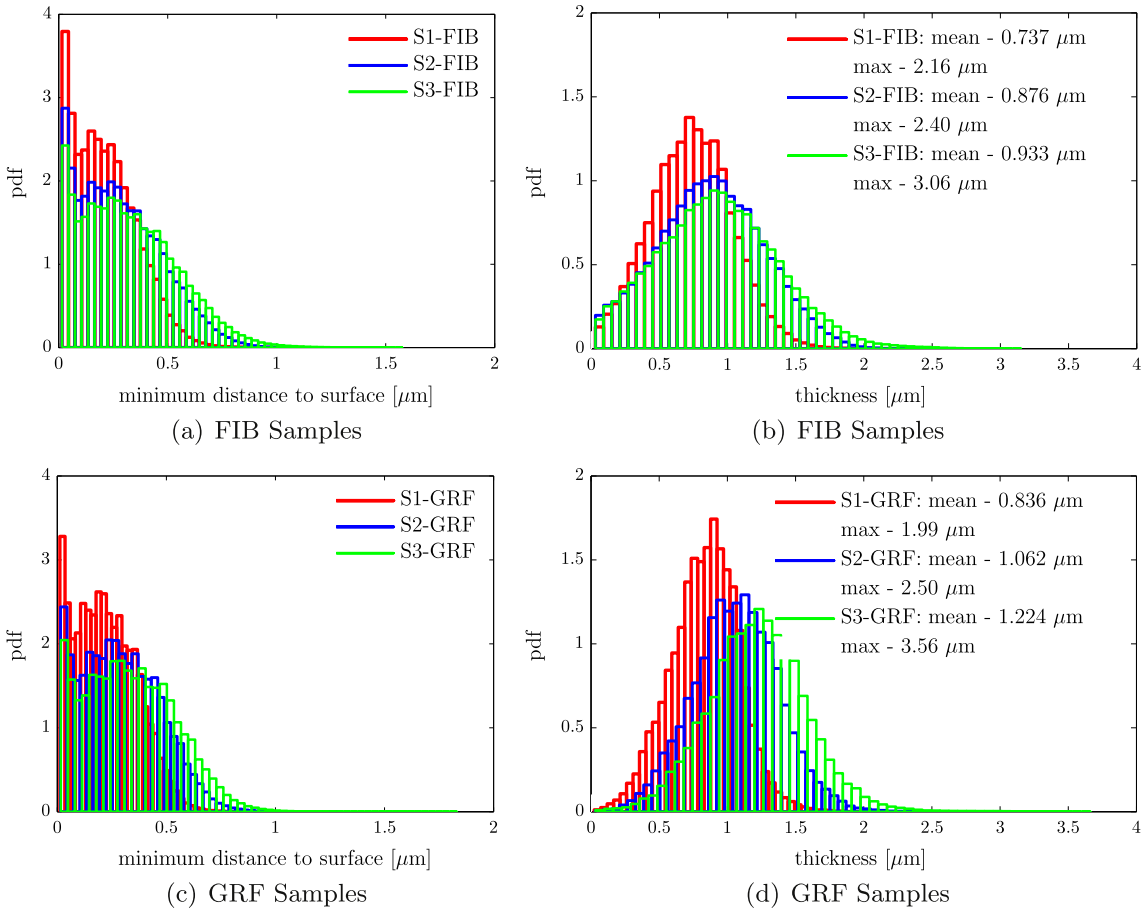

Fig. 7. Probability density functions (pdf) for minimum distance field and thickness distribution for (a, b) real microstructures and (c, d) synthetic GRF microstructures.

directions did not change the results within the statistical deviation. Assuming isotropic linear Fourier's law for both phases, the steady state heat conduction problem is solved, resulting in the microscopic temperature and heat flux distributions within the MVE, Fig. 9. The macroscopic effective heat flux is computed as the volume average of the microscopic heat flux. Relating the computed macroscopic heat flux to the macroscopic prescribed temperature gradient results in the effective thermal conductivity.

For the mechanical simulations, uniaxial tensile loading was applied on the MVEs. To this end, displacements have been prescribed in the vertical direction, combined with the periodic boundary conditions in the three spatial directions. The same remarks as above with respect to the periodic boundary conditions apply to the mechanical simulations as well. It has again been verified that prescribing tensile loading in other directions did not change the results. Isotropic linear elastic Hooke's law was assumed for both phases. Solving the equilibrium problem results in the distribution of displacement and stress fields within the MVE, Fig. 9. Relating the prescribed overall axial tensile strain to the reaction force corresponding to the overall uniaxial stress provides the effective Young's modulus.

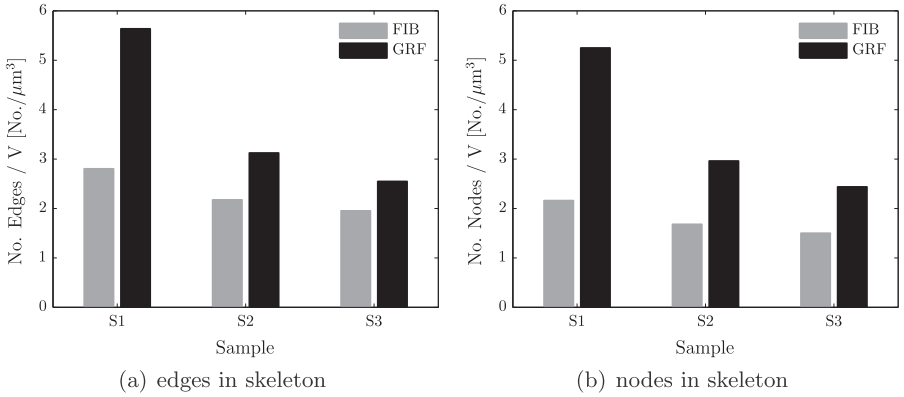

Fig. 8. Skeleton analysis for real and artificial microstructures.

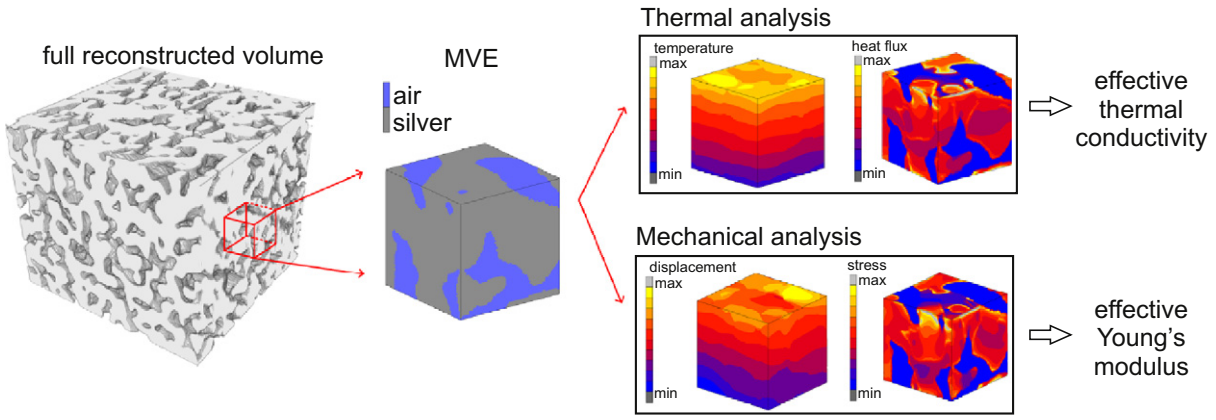

Fig. 9. Overview of the numerical analysis: an MVE is created from the 3D segmented microstructure followed by the thermal or mechanical finite element analyses from which the effective properties are computed.

4.2. Statistical micromechanics

Effective material properties are also computed using statistical micromechanics theories to illustrate their applicability in accurately determining microstructure statistics-property relations. Statistical micromechanics theories have been developed over the past half century, and details of these developments are presented in books by Milton [15] and Torquato [16].

In this work, third-order statistical micromechanics models are utilized for computing the effective thermal conductivity and elastic constants. These estimates depend on the individual phase properties (κ_i, K_i, and G_i being the thermal conductivity, bulk modulus, and shear modulus of material phase i), the material volume fractions c_i, and microstructural parameters ζ_i and η_i that are functions of the one-, two-, and three-point probability functions. For the effective thermal conductivity, the expression obtained through the strong-contrast expansion derived by Torquato is utilized (See Eq. (20.84) in [16]). This expression is given as (for $\kappa_2/\kappa_1 = 0$)

$$\kappa_e/\kappa_1 = 1 - \frac{d\, c_2}{d - c_1 - \zeta_2}. \tag{6}$$

For the porous microstructures considered here, κ_1 is the effective thermal conductivity of the solid phase and $\kappa_2 = 0$ (perfectly insulating pore phase), d is the dimension of the structure ($d = 3$ in this work), and the microstructural parameter ζ_2 is given as

$$\zeta_2 = \frac{9}{2c_2c_1}\int_0^\infty\int_0^\infty\int_{-1}^{1}\frac{3\cos^2\theta - 1}{2r_1r_2}\tilde{S}_{222}(r_1, r_2, \theta)\mathrm{d}(\cos\theta)\, \mathrm{d}r_1\, \mathrm{d}r_2, \tag{7}$$

where

$$\tilde{S}_{222}(r_1, r_2, \theta) = \frac{S_{222}(r_1, r_2, \theta) - S_{22}(r_1)S_{22}(r_2)}{c_2}. \tag{8}$$

$S_{222}(r_1, r_2, \theta)$ and $S_{22}(r)$ are the three- and two-point probability functions (see Eq. (5)). As mentioned by Torquato, this expression perturbs about the self-consistent estimate of Bruggeman [6] and Landauer [33,34] and is expected to yield an accurate estimate for phase-inversion-symmetric structures. Phase-inversion-symmetric morphologies, e.g. symmetric cell materials and certain GRF models, denote structures where microstructural parameters of phase 1 are equivalent to the microstructural parameters of phase 2 when the volume fraction of phase 1 is $1-c_1$. For the effective elastic constants, the strong contrast expansion derived by Torquato (see Eqs. (4.1)–(4.5) in [35]) is considered. The bulk and shear moduli assuming no stiffness in the pore phase ($K_2 = G_2 = 0$) are given as

$$\frac{K_e}{K_1} = \frac{1 - c_2 - \frac{15K_1}{9K_1+8G_1}c_1\zeta_2}{1 + \frac{3K_1}{4G_1}c_2 - \frac{15K_1}{9K_1+8G_1}c_1\zeta_2}, \tag{9}$$

and

$$\frac{G_e}{G_1} = \frac{1 - c_2 - \frac{3K_1}{9K_1+8G_1}c_1\zeta_2 - 6\left[\frac{3K_1+G_1}{9K_1+8G_1}\right]^2 c_1\eta_2 - \frac{30G_1(2K_1+3G_1)}{(9K_1+8G_1)^2}c_1\zeta_2}{1 + \frac{6(K_1+2G_1)}{9K_1+8G_1}c_2 - \frac{3K_1}{9K_1+8G_1}c_1\zeta_2 - \cdots}, \tag{10}$$

where

$$\eta_2 = \frac{5\zeta_2}{21} + \frac{150}{7c_2c_1}\int_0^\infty\int_0^\infty\int_{-1}^{1}\frac{P_4(\cos\theta)}{r_1r_2}\tilde{S}_{222}\mathrm{d}(\cos\theta)\mathrm{d}r_1\mathrm{d}r_2. \tag{11}$$

Here $P_4(\cos\theta)$ is the fourth order Legendre polynomial. In addition, these three-point approximations are also compared to the commonly used Hashin-Shtrikman bounds (HS) [36,37]. Note that the HS bounds are second-order bounds and are only a function of the material volume fraction and thus cannot differentiate among varying microstructures.

Determining the microstructural parameters ζ_i and η_i in these higher order models is often difficult for a wide range of microstructures, as analytical expressions of the n-point probability functions are often lacking. Symmetric-cell and GRF are among the models for which the probability functions have been formulated analytically, and the microstructural parameters have been evaluated and presented in the literature [16,23]. Recently, accurate methods have been reported for computing these parameters directly from three-dimensional microstructures [18,19]. In this work, we compute the third-order effective properties utilizing parameters available in the literature for symmetric-cell GRF models and compare them to the computational homogenization results.

Table 3
Material properties of silver and "air" used in the numerical simulations.

Phase	Thermal conductivity [W/(mK)]	Young's modulus [MPa]	Poisson ratio [–]
Silver	419	83,000	0.37
"Air"	1×10^{-5}	1×10^{-5}	0

5. Results

In this section, we report the microstructure statistics-property relations for both the computational homogenization and statistical micromechanics approaches. Regarding the statistical micromechanics predictions, the HS upper bound and the third-order estimates for four unique classes of ideal microstructures are considered. Note that the microstructural parameters for the symmetric cell material models (spherical, cubical, and needle-like cells) are summarized in Chapter 22 of [16], and the microstructural data for the Gaussian random field 1-cut model is presented in Table I and Table IX of [23] (Model III). Fig. 10 shows the predictions of the effective thermal conductivity, κ_e, normalized by the thermal conductivity of the solid phase, κ_s, as a function of the solid material volume fraction. Note that the third-order estimates deviate at most by 5% for the microstructural models considered in the volume fraction range of interest. In the previous sections, we have shown that the GRF model captures many of the relevant structural features of the real sintered microstructures. In contrast, the structural characteristics of the symmetric cell materials are significantly different despite similar effective property predictions. Symmetric cell microstructures are generated through subdividing the volume into cells of a particular shape, followed by random assignment of material phases. The cubical symmetric cell material, for example, is composed of tiled cubes where each cube is randomly chosen to be a solid or a void. Thus, this microstructure results in a saturation of the two-point probability function at one cell length (see [16]), which is significantly different from the two-point probability function observed for GRF models and the sintered silver paste material (see Fig. 5). This suggests that GRF models have a longer correlation length. Moreover, while there is little differentiation in the effective material predictions of the symmetric cell and GRF models for linear materials, more complex loading regimes and nonlinear irreversible material behavior are likely to reveal significant differences. The importance of a large correlation length, and thus large MVE size, has been shown for nonlinear material softening in [38]. For future study of these materials, we have shown that a GRF material model is a good synthetic microstructure for representing these sintered silver pastes.

In addition to the statistical micromechanics estimates, we also consider direct simulation of the real microstructures. For the real samples, the finite element simulations on 12 MVEs per sample (S1, S2, and S3) were performed as described in Section 4.1. Each MVE contained 110^3 hexahedral elements (1.331 M elements). The mean results of the effective thermal conductivity obtained through the MVE simulations are represented by the three markers (filled circle, triangle, and diamond for sample S1, S2, and S3, respectively), and the gray shaded ellipses represent one standard deviation of the distribution of 12 FEM simulations performed for each sample. This ellipse is determined from the covariance matrix of the effective thermal conductivity/volume fraction data. Note that these distributions overlap significantly with the idealized microstructural models, illustrating the good agreement between the two modeling approaches. The differences in the volume fraction of each sample contribute most to the difference in the effective properties, while the differences in the microstructural character among the samples play a secondary role.

Similar to the effective thermal conductivity, the effective Young's modulus, E_e, is also computed using both modeling approaches. The HS upper bound, the third-order estimates, and the FEM computational homogenization results as a function of the material volume fraction are presented in Fig. 11. The trends in predictions of the effective thermal conductivity described above are similar to the trends in the effective Young's modulus. However, the third-order estimates among the four ideal microstructures vary at most by 10% for the volume fraction range of interest, indicating that the Young's modulus is more sensitive to morphology for these types of microstructures. This sensitivity is also reflected in the larger spread in the standard deviation ellipses of the FEM data.

The good agreement between the computational homogenization FEM results, used here as the reference, and the analytical higher-order statistical micromechanics estimates shows that the synthetic models can be used for the prediction of the linear effective material properties of the sintered silver interconnect material in the considered range of volume fractions, thus reducing the material development efforts. Finally, it is remarked that the model predictions are in good agreement with the experimentally measured ranges of thermal and mechanical properties [39], although the experimental data show a significant spread between different publications [13,40-42], which can be attributed to large variations in processing conditions (bulk material versus an interconnect), the presence of the defects (e.g. large voids) and the capabilities of measurement techniques to deal with small porous samples.

6. Conclusions

In this paper, a methodology for establishing microstructure statistics-property relations has been presented and applied to a sintered silver particle-based interconnect material for high power electronic applications. The novel original feature of this approach is the combination of the statistical morphological measures of real and synthetic microstructures with the higher-order statistical

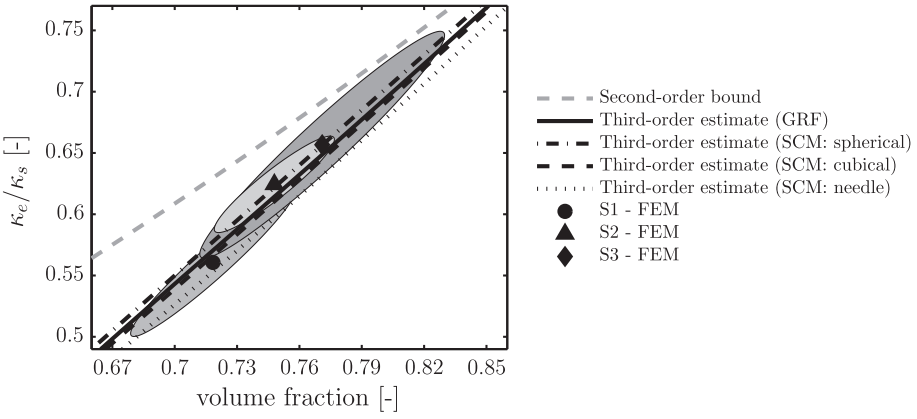

Fig. 10. Second-order bound and third-order estimates for effective thermal conductivity, κ_e, normalized by the thermal conductivity of the solid phase, κ_s, as function of the material volume fraction for porous silver samples.

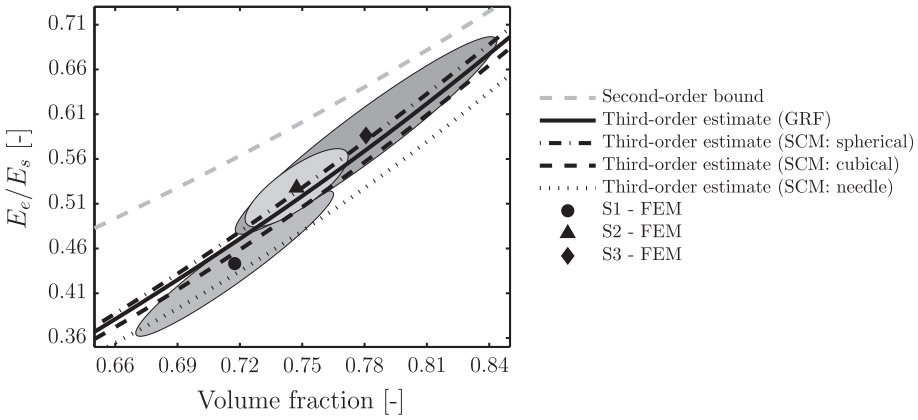

Fig. 11. Second-order bound and third-order estimates for effective Young's modulus, E_e, normalized by the Young's modulus of the solid phase, E_s, as function of the material volume fraction for porous silver samples.

micromechanics and direct finite element computational homogenization. The main steps and conclusions of this contribution can be summarized as follows.

- Three sintered silver samples were produced under different processing conditions, i.e. sintering temperatures of 230 °C (sample S1), 280 °C (sample S2) and 330 °C (sample S3). The complex 3D interconnected microstructures of these samples were revealed by the SEM-FIB technique, i.e. through the reconstruction of 3D structure based on Scanning Electron (SEM) microscopy images of sample surfaces revealed by sequential Focussed Ion Beam (FIB) milling.
- The statistical analysis of the microstructural features has revealed that increasing sintering temperature leads to higher volume fraction of the solid phase (lower porosity). More interestingly, the mean ligament thickness and the width of ligament thickness distribution have increased between the samples S1 and S2 and was statistically almost equivalent between the samples S2 and S3.
- In order to better understand the microstructure statistics-property relations for these complex morphologies, synthetic microstructures have been generated based on Gaussian random field models, having a well defined analytical description. The statistical characteristics of the real samples and the synthetic models have been analysed and shown to have a good correspondence.
- The effective thermal conductivity and Young's modulus of the considered sintered silver materials have been computed using the computational homogenization approach based on the finite element models of the 3D microstructures. The results show that the effective thermal conductivity of this 3D interconnected microstructures, in the considered range of volume fractions, is mostly determined by the volume fraction, with the microstructural variations playing a secondary role. The Young's modulus, on the other hand, is more sensitive to the local microstructural features.
- The computed effective properties have been compared to the predictions based on the analytical higher-order statistical micromechanics estimates for the synthetic microstructures, demonstrating very good agreement. This shows that the linear effective properties of these materials can be predicted based on the analytical estimates for synthetic morphologies.

The results of this work can be used for increasing efficiency of material development of sintered silver thermal interface materials by (partially) replacing the costly material characterization by analytical predictions. In addition, the approach proposed in this work, based on the combination of statistical micromechanics and computational homogenization, can be applied for other materials, leading to the identification of suitable synthetic models for establishing microstructure statistics-property relations.

Acknowledgments

The authors are grateful to Dr. Sebastian Fritzsche from Heraeus for providing the materials for this study. This work was partially supported by the NANOTHERM project co-funded by the European Commission under the "Information and Communication Technologies", Seventh Framework Program, Grant Agreement No.318117.

References

[1] X. Tong, Advanced Materials for Thermal Management of Electronic Packaging, Springer. 2011.
[2] T. Wang, X. Chen, G. Lu, G.-Y. Lei, Low-temperature sintering with nano-silver paste in die-attached interconnection, J. Electron. Mater. 36 (2007) 1333–1340.
[3] K.S. Siow, Are sintered silver joints ready for use as interconnect material in microelectronic packaging? J. Electron. Mater. 43 (4) (2014) 947–961.
[4] S.A. Paknejad, A. Mansourian, Y. Noh, K. Khtatba, S.H. Mannan, Thermally stable high temperature die attach solution, Mater. Des. 89 (2016) 1310–1314.
[5] K. Matouš, M.G.D. Geers, V.G. Kouznetsova, A. Gillman, A review of predictive nonlinear theories for multiscale modeling of heterogeneous materials, J. Comput. Phys. 330 (2017) 192–220.
[6] D.A.G. von Bruggeman, Berechnung verschiedener physikalischer Konstanten von heterogenen Substanzen. I. Dielektrizitätskonstanten und Leitfähigkeiten der Mischkörper aus isotropen Substanzen, Annalen der physik 416 (7) (1935) 636–664.
[7] L.E. Nielsen, The thermal and electrical conductivity of two-phase systems, Ind. Eng. Chem. Fundam. 13 (1) (1974) 17–20.
[8] C.-W. Nan, R. Birringer, D.R. Clarke, H. Gleiter, Effective thermal conductivity of particulate composites with interfacial thermal resistance, J. Appl. Phys. 81 (10) (1997) 6692–6699.
[9] J. Ordonez-Miranda, J.J. Alvarado-Gil, Effect of the pore shape on the thermal conductivity of porous media, J. Mater. Sci. 47 (18) (2012) 6733–6740.
[10] A. El Moumen, T. Kanit, A. Imad, H. El Minor, Computational thermal conductivity in porous materials using homogenization techniques: numerical and statistical approaches, Comput. Mater. Sci. 97 (2015) 148–158.
[11] R. Bolot, G. Antou, G. Montavon, C. Coddet, A two-dimensional heat transfer model for thermal barrier coating average thermal conductivity computation, Numer. Heat Transfer, Part A: Appl. 47 (9) (2005) 875–898.
[12] S. Grandjean, J. Absi, D.S. Smith, Numerical calculations of the thermal conductivity of porous ceramics based on micrographs, J. Eur. Ceram. Soc. 26 (13) (2006) 2669–2676.
[13] J. Ordonez-Miranda, M. Hermens, I. Nikitin, V.G. Kouznetsova, O. van der Sluis, M. Abo Ras, J.S. Reparaz, M.R. Wagner, M. Sledzinska, J. Gomis-Bresco, C.M. Sotomayor Torres, B. Wunderle, S. Volz, Measurement and modeling of the effective thermal conductivity of sintered silver pastes, Int. J. Therm. Sci. 108 (2016) 185–194.

[14] G. Laschet, J. Sauerhering, O. Reutter, T. Fend, J. Scheele, Effective permeability and thermal conductivity of open-cell metallic foams via homogenization on a microstructure model, Comput. Mater. Sci. 45 (3) (2009) 597–603.
[15] G.W. Milton, The Theory of Composites, Cambridge University Press. 2002.
[16] S. Torquato, Random Heterogeneous Materials: Microstructure and Macroscopic Properties, 16. Springer-Verlag New York. 2002.
[17] A. Gillman, K. Matouš, S. Atkinson, Microstructure-statistics-property relations of anisotropic polydisperse particulate composites using tomography, Phys. Rev. E 87 (2) (2013) 022208.
[18] A. Gillman, K. Matouš, Third-order model of thermal conductivity for random polydisperse particulate materials using well-resolved statistical descriptions from tomography, Phys. Lett. A 378 (41) (2014) 3070–3073.
[19] A. Gillman, G. Amadio, K. Matouš, T.L. Jackson, Third-order thermo-mechanical properties for packs of Platonic solids using statistical micromechanics, Proceedings of the Royal Society of London A: Mathematical, Physical and Engineering Sciences, 471, The Royal Society. 2015, pp. 20150060. 2177.
[20] Heraeus Materials Technology GmbH and Co., (http://www.heraeus.com).
[21] R.K. Bansal, A. Kubis, R. Hull, J.M. Fitz-Gerald, High-resolution three-dimensional reconstruction: a combined scanning electron microscope and focused ion-beam approach, J. Vac. Sci. Technol. B 24 (2) (2006) 554–561.
[22] C.E. Shuck, M. Frazee, A. Gillman, M.T. Beason, I.E. Gunduz, K. Matouš, R. Winarski, A.S. Mukasyan, X-ray nanotomography and focused-ion-beam sectioning for quantitative three-dimensional analysis of nanocomposites, J. Synchrotron Radiat. 23 (4). (2016)
[23] A.P. Roberts, M. Teubner, Transport properties of heterogeneous materials derived from Gaussian random fields: bounds and simulation, Phys. Rev. E 51 (5) (1995) 4141.
[24] M.A. Knackstedt, A.P. Roberts, Morphology and macroscopic properties of conducting polymer blends, Macromolecules 29 (4) (1996) 1369–1371.
[25] A.P. Roberts, Morphology and thermal conductivity of model organic aerogels, Phys. Rev. E 55 (2) (1997) R1286–R1289.
[26] A.P. Roberts, E.J. Garboczi, Computation of the linear elastic properties of random porous materials with a wide variety of microstructure, Proceedings of the Royal Society of London A: Mathematical, Physical and Engineering Sciences, 458, 2002, pp. 1033–1054. 2021.
[27] H. Lee, M. Brandyberry, A. Tudor, K. Matouš, Three-dimensional reconstruction of statistically optimal unit cells of polydisperse particulate composites from microtomography, Phys. Rev. E 80 (6) (2009) 061301.
[28] C. Fouard, G. Malandain, S. Prohaska, M. Westerhoff, Blockwise processing applied to brain microvascular network study, IEEE Trans. Med. Imaging 25 (10) (2006) 1319–1328.
[29] M.G.D. Geers, V.G. Kouznetsova, W.A.M. Brekelmans, Multi-scale computational homogenization: trends & challenges, J. Comput. Appl. Math. 234 (7) (2010) 2175–2182.
[30] M.G.D. Geers, V.G. Kouznetsova, K. Matouš, J. Yvonnet, Homogenization methods and multiscale modeling: non-linear problems, in: E. Stein, R de Borst, T. Hughes (Eds.), Encyclopedia of Computational Mechanics, John Wiley and Sons, NY, 2017,
[31] I. Özdemir, W.A.M. Brekelmans, M.G.D. Geers, Computational homogenization for heat conduction in heterogeneous solids, Int. J. Numer. Methods Eng. 73 (2) (2008) 185–204.
[32] T. Kanit, S. Forest, I. Galliet, V. Mounoury, D. Jeulin, Determination of the size of the representative volume element for random composites: statistical and numerical approach, Int. J. Solids Struct. 40 (2003) 3647–3679.
[33] R. Landauer, The electrical resistance of binary metallic mixtures, J. Appl. Phys. 23 (7) (1952) 779–784.
[34] R. Landauer, Electrical conductivity in inhomogeneous media, AIP Conference Proceedings: Electrical transport and optical properties of inhomogeneous media 40 (1) (1978) 2–45.
[35] S. Torquato, Effective stiffness tensor of composite media: II. Applications to isotropic dispersions, J. Mech. Phys. Solids 46 (8) (1998) 1411–1440.
[36] Z. Hashin, S. Shtrikman, A variational approach to the theory of the effective magnetic permeability of multiphase materials, J. Appl. Phys. 33 (10) (1962) 3125–3131.
[37] Z. Hashin, S. Shtrikman, A variational approach to the theory of the elastic behaviour of multiphase materials, J. Mech. Phys. Solids 11 (2) (1963) 127–140.
[38] M. Mosby, K. Matouš, On mechanics and material length scales of failure in heterogeneous interfaces using a finite strain high performance solver, Model. Simul. Mater. Sci. Eng. 23 (8) (2015) 085014.
[39] A.A. Wereszczak, D.J. Vuono, H. Wang, M.K. Ferber, Properties of bulk sintered silver as a function of porosity, Technical Report ORNL/TM-2012/130, Oak Ridge National Laboratory, 2012,
[40] J.G. Bai, Z.Z. Zhang, J.N. Calata, G.-Q. Lu, Low-temperature sintered nanoscale silver as a novel semiconductor device-metallized substrate interconnect material, IEEE Trans. Compon. Packag. Technol. 29 (3) (2006) 589–593.
[41] D. Yu, X. Chen, G. Chen, G. Lu, Z. Wang, Applying Anand model to low-temperature sintered nanoscale silver paste chip attachment, Mater. Des. 30 (10) (2009) 4574–4579.
[42] V. Caccuri, X. Milhet, P. Gadaud, D. Bertheau, M. Gerland, Mechanical properties of sintered Ag as a new material for die bonding: influence of the density, J. Electron. Mater. 43 (12) (2014) 4510–4514.